Research Square

Preprints are preliminary reports that have not undergone peer review.
They should not be considered conclusive, used to inform clinical practice,
or referenced by the media as validated information.

Engineering High-Performance ZnO/P3HT Hybrid Heterostructure Diodes: Systematic Layer-Dependent Optimization of Structural, Morphological, and Optical Properties

L. Merzougui
USTOMB University
M. Benhaliliba
mbenhaliliba@gmail.com

USTOMB University
A. Souidi
Université de Saida Dr Moulay Tahar
K. Dris
USTOMB University
A. Ayeshamariam
Khadir Mohideen College, Bharathidasan University

Research Article

Keywords: Hybrid solar cells, ZnO thin films, P3HT, sol-gel method, heterostructure optimization, organic-inorganic interface

Posted Date: November 20th, 2026

DOI: https://doi.org/10.21203/rs.3.rs-11574231/v1

License: This work is licensed under a Creative Commons Attribution 4.0 International License.
Read Full License

Additional Declarations: No competing interests reported.

Engineering High-Performance ZnO/P3HT Hybrid Heterostructure Diodes: Systematic Layer-Dependent Optimization of Structural, Morphological, and Optical Properties

L. Merzougui[1], M. Benhaliliba[1] *, M.A. Souidi[1,2], K. Dris[1], A. Ayeshamariam[3]

[1]Film Device Fabrication-Characterization and Application FDFCA Research Group USTOMB University, 31130, Oran, Algeria.

[2]MIT Faculty, Tahar Moulay University, Saida, Algeria

[3]Department of Physics, Khadir Mohideen College, (Affiliated to Bharathidasan University, Tiruchirappalli), Adirampattinam, Tamil Nadu 614701, India.

**Corresponding author:*
mbenhaliliba@gmail.com

Abstract

Hybrid organic-inorganic solar cells combining zinc oxide (ZnO) and poly(3-hexylthiophene) (P3HT) represent a promising avenue for cost-effective photovoltaic technology. This study systematically investigates the fabrication and optimization of ZnO/P3HT heterostructure diodes prepared via sol-gel spin-coating on borosilicate glass substrates. We examine the effects of layer number (4, 6, 8, and 10 layers for ZnO; 2, 3, 4, and 5 layers for P3HT) and calcination temperature on structural, morphological, and optical properties. X-ray diffraction analysis reveals that 8-layer ZnO films yield optimal crystallite size (36.11 nm), minimum internal strain (3.4×10^{-3}), and superior hexagonal wurtzite phase formation. For P3HT, 4-layer configuration achieves maximum lamellar ordering with optimal (100) peak intensity (1386.30 cts) and d-spacing of 18.63 Å. Scanning electron microscopy confirms homogeneous, continuous film morphology for optimized configurations. UV-Vis spectroscopy demonstrates excellent optical transparency (>98% at 800 nm) and optimal bandgap (3.335 eV) for 8-layer ZnO. A thermally-separated fabrication protocol addresses the thermal incompatibility between ZnO calcination (450°C) and P3HT processing (<195°C degradation threshold). The optimized ZnO (8 layers) /P3HT (4 layers) architecture establishes fundamental design principles for high-performance hybrid photovoltaic devices.

Keywords : Hybrid solar cells, ZnO thin films, P3HT, sol-gel method, heterostructure optimization, organic-inorganic interface

1. Introduction

Hybrid organic-inorganic photovoltaic devices offer compelling advantages over conventional silicon, including mechanical flexibility and low-cost, solution-processable manufacturing. Among these architectures, the combination of metal oxide semiconductors with conjugated polymers, specifically the ZnO/P3HT heterojunction, has garnered significant interest. Zinc oxide (ZnO) is an ideal n-type component due to its wide bandgap, high transparency, electron mobility, and environmental stability [1–3], while poly(3-hexylthiophene) (P3HT) serves as the primary light-absorbing and hole-transporting material.

However, realizing high-performance ZnO/P3HT devices in a conventional structure (where ZnO is deposited first and requires high-temperature processing) presents a critical fabrication challenge: thermal incompatibility. Optimal crystallinity for the ZnO layer requires calcination (400-550°C), whereas P3HT exhibits thermal degradation starting at approximately 195 °C [4]. Furthermore, precise optimization of layer thickness is essential, as the configuration must balance sufficient light absorption with the constraints of exciton diffusion length and increased recombination losses observed in layers exceeding five [5],[6].

While previous studies have optimized the individual components, comprehensive investigations systematically correlating processing parameters with the overall structural and morphological properties of the complete heterostructure remain limited. Inverting the device architecture is the primary strategy employed to decouple these conflicting thermal requirements.

This work presents a systematic investigation into the optimized fabrication of inverted ZnO/P3HT heterostructures using sol-gel spin-coating. We analyze the influence of layer number on material properties through multi-technique characterization (XRD, SEM, UV-Vis spectroscopy) to establish definitive structure-property relationships and provide robust design principles for high-performance organic-inorganic photovoltaic devices.

2. Materials and Methods

2.1 Materials

Zinc acetate dihydrate [$Zn(CH_3COO)_2 \cdot 2H_2O$, 99.9% purity], absolute ethanol (≥99.8%), and diethanolamine (DEA, 99%) were obtained from commercial suppliers and used without further purification. Regioregular poly(3-hexylthiophene-2,5-diyl) (P3HT, Mw = 50,000-70,000 g/mol,

regioregularity >95%) and anhydrous toluene (99.8%) were procured from commercial sources. Borosilicate glass substrates (25.4 × 76.2 mm, thickness 1.0-1.2 mm) were selected based on optical transparency (>90% transmittance at 650 nm) [1–3], electrical resistivity (>10^{12} Ω·cm), and thermal expansion coefficient compatibility (3.3 × 10^{-6} K^{-1}) [7] with ZnO films (4.3- 5.6 × 10^{-6} K^{-1}) [8].

2.2 Substrate Cleaning Protocol

Glass substrates underwent a rigorous cleaning procedure, as detailed in **Figure 1**, essential for achieving contamination-free surfaces critical for the uniform nucleation and reliable adhesion of thin films [9],[10]. This comprehensive protocol involved several sequential stages: Substrates were initially washed with mild soap followed by copious rinsing with running water, and then a rinse with distilled water. Subsequently, they were subjected to a 10-minute ultrasonic treatment in an acetone bath to effectively remove bulk organic residues, immediately followed by an intermediate rinse with distilled water. A second 10-minute ultrasonic treatment was then performed in ethanol for the final elimination of any trace organic contaminants. Upon removal from the final bath, a final rinse with distilled water was executed. The substrates were then rapidly dried using a jet of nitrogen gas to prevent recontamination, and finally received a thermal treatment in an open-air oven at 200 °C for 10 minutes to eliminate residual moisture. This method ensures the realization of atomically clean surfaces with minimal particulate and organic contamination, thereby optimizing conditions for subsequent high-quality deposition processes.

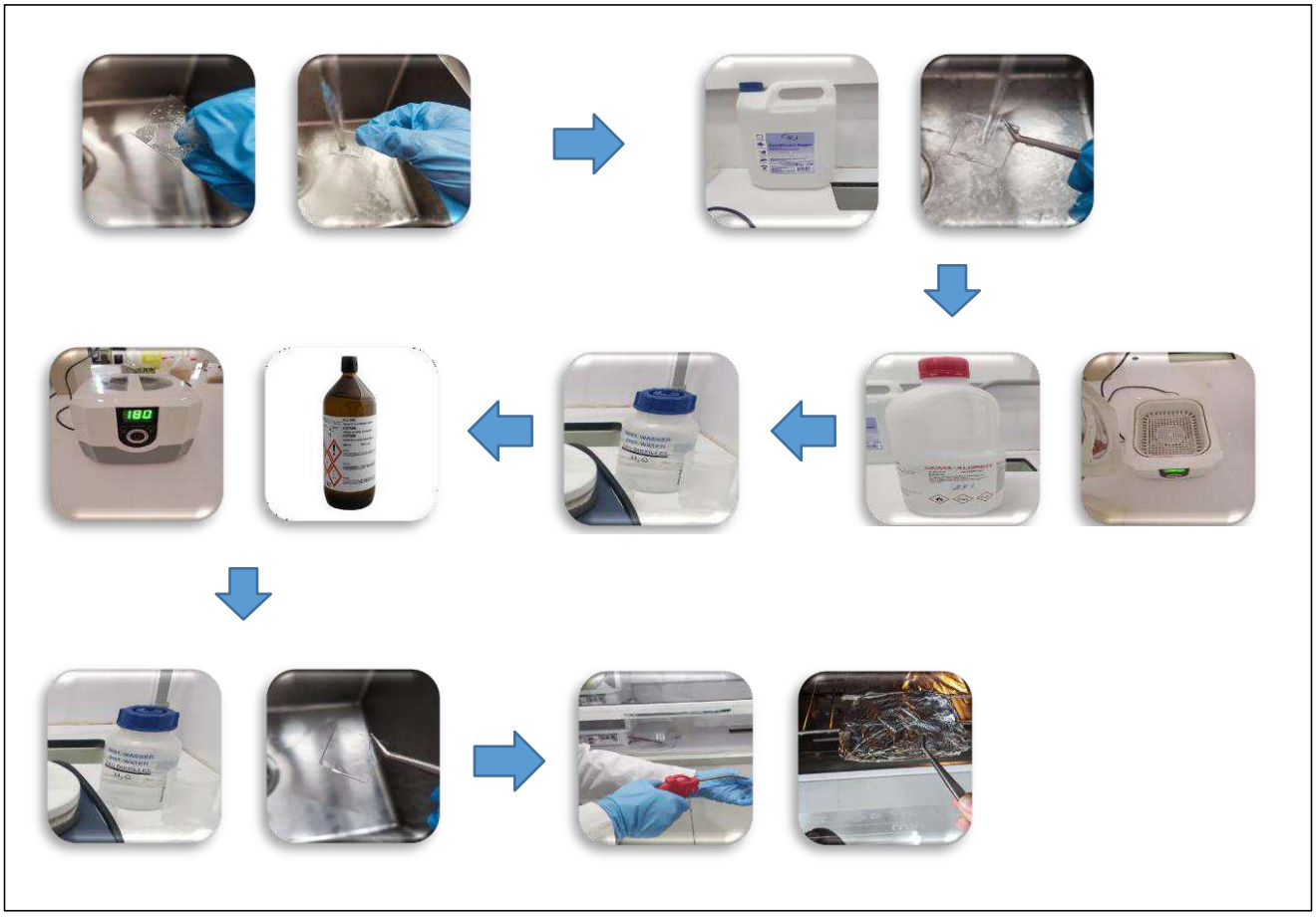

Figure 1 : Cleaning Protocol of Substrates Before Deposition.

2.3 ZnO Sol-Gel Preparation

ZnO precursor solutions were prepared following optimized sol-gel protocols. Zinc acetate dihydrate was dissolved in absolute ethanol to achieve 0.5 M concentration. Diethanolamine (DEA) was added as stabilizing agent in 1:1 molar ratio with zinc acetate. The mixture underwent continuous magnetic stirring at 600 RPM and 60°C for 90 minutes in sealed containers to prevent solvent evaporation, yielding homogeneous transparent solutions. The controlled thermal and mechanical treatment promotes complete dissolution and sol formation.

2.4 P3HT Solution Preparation

P3HT solutions were prepared by dissolving 0.05 g high-purity P3HT powder in 5 mL anhydrous toluene (10 mg/mL concentration) as depicted in **Figure 2**. Dissolution occurred under continuous magnetic stirring at 600 RPM and 40°C for 2.5 hours in sealed containers until homogeneous dark orange solutions formed without visible particulates. The moderate temperature prevents polymer degradation while providing sufficient thermal energy for chain disentanglement.



Figure 2 : Core Reactants and Final P3HT Solution : (a) High-purity P3HT powder ; (b) Anhydrous Toluene solvant ; and (c) Resulting solution prior to filtration.

2.5 Device Architecture

The structure of hybrid heterostructure diodes (organic/inorganic) (**Figure 3**) were fabricated using the sol gel and spin-coating technique

Figure 3 : Schematic representation of the hybrid ZnO/P3HT heterostructure.

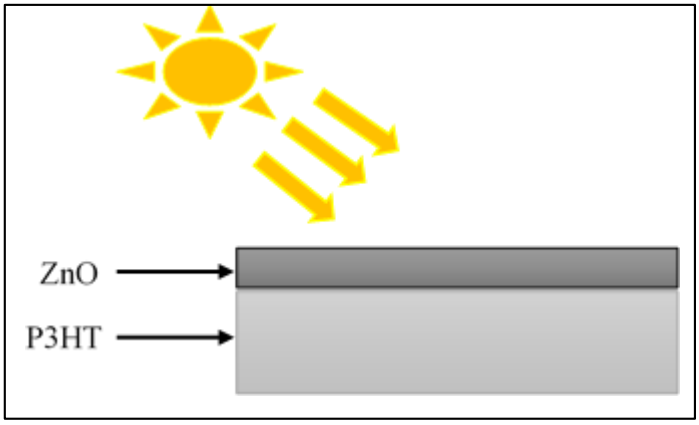

3. Thin Film Deposition

3.1 ZnO Film Fabrication

ZnO thin films were deposited via spin-coating at 3000 RPM for 30 seconds [11–13]. Multilayer films (4, 6, 8, and 10 layers) were fabricated with intermediate drying at 200°C for 10 minutes between successive layers to promote solvent evaporation and partial densification. Following complete deposition, films underwent calcination at 450°C for 2 hours in ambient atmosphere with controlled heating rate (12°C/hour, equivalent to 1°C per 5 minutes) to ensure gradual organic residue removal, optimal crystallization, and stress minimization [1–3, 14–16]. The slow heating rate prevents crack formation from rapid gas evolution and promotes uniform densification. The calcination temperature of 450°C for 2 hours was selected based on literature optimization studies demonstrating optimal crystalline quality for ZnO films [17]. The process is illustrated in **Figure 4**.

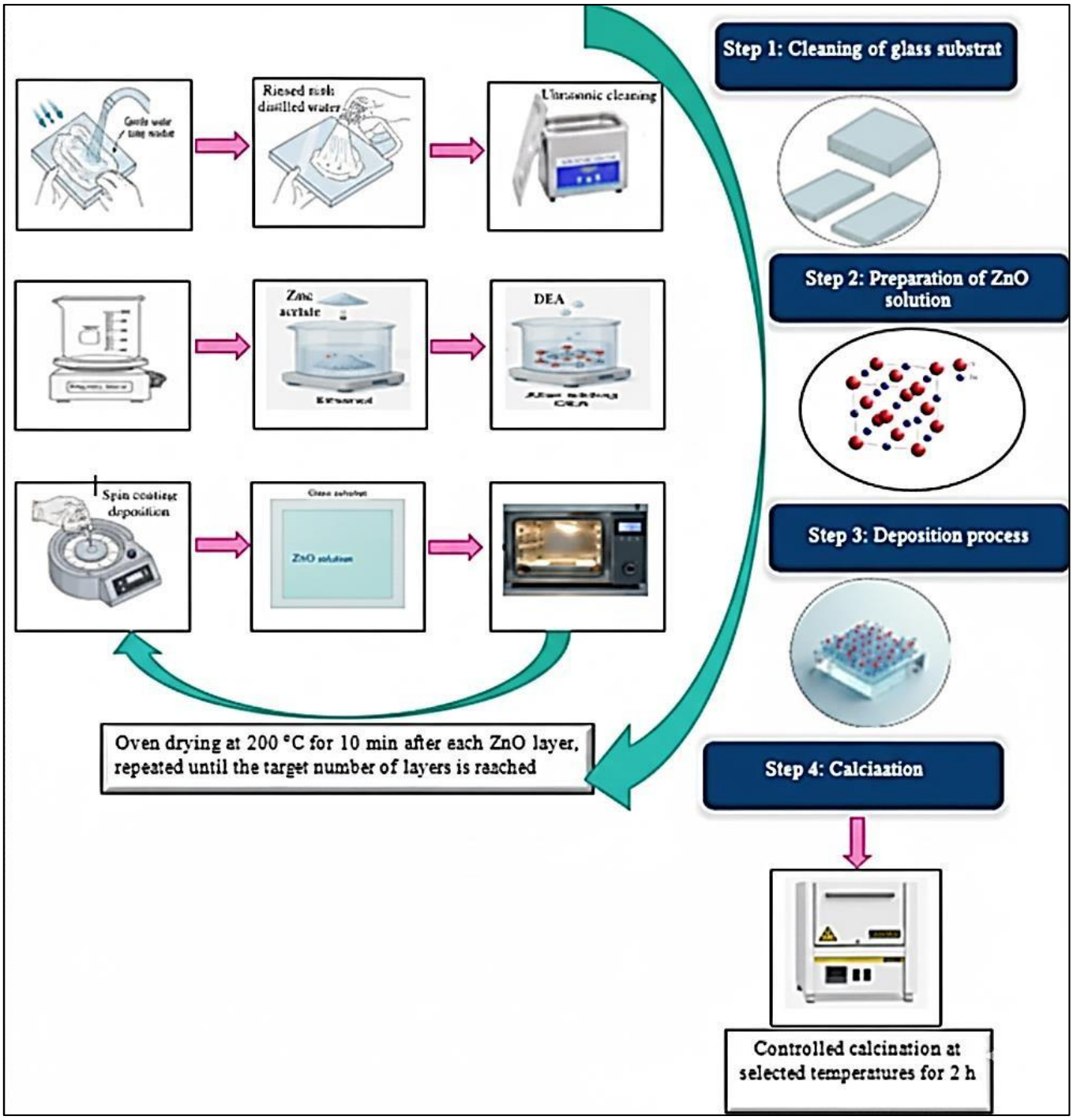

Figure 4 : Flowchart Of The ZnO Thin Film Synthesic Process.

3.2 P3HT Film Fabrication

P3HT films (2, 3, 4, and 5 layers) were deposited via spin-coating at 2500 RPM for 30 seconds on ZnO-coated or bare glass substrates. Each layer underwent intermediate thermal treatment at

100°C for 3 minutes to remove residual solvent while preventing interlayer mixing. Complete multilayer assemblies received final annealing at 130°C for 10 minutes as displayed in **Figure 5a** to optimize molecular ordering and crystallinity [18] while remaining below the thermal degradation threshold (~195°C) [19], resulting in uniform films as sketched in **Figure 5b** suitable for device integration.

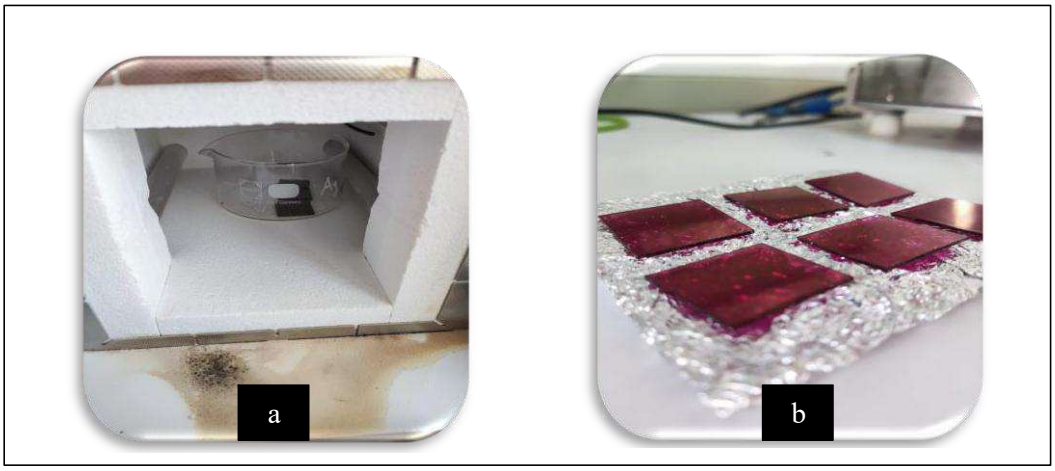

Figure 5 : Thermal treatment process : furnace used for calcination (a) and spin-coated resulting films (b).

4. Characterization Techniques

4.1 Structural Analysis

X-ray diffraction (XRD) measurements were performed using a Rigaku MiniFlex 600 diffractometer (**Figure 6**) with Cu Kα radiation (λ = 1.5406 Å) operating at 40 kV and 15 mA. Diffraction patterns were recorded in θ-2θ configuration over 2θ range of 5-80° with 0.02° step size and 1 second counting time per step [20,21]. Phase identification utilized JCPDS reference cards (ZnO : 036-1451 hexagonal wurtzite ; P3HT : 00-052-2366 orthorhombic) [22].



Figure 6 : Rigaku MiniFlex 600 X-ray Diffractometer Used for Structural Analysis

Crystallite sizes were calculated using the Scherrer equation (Eq. 1) [23]:

$$D = K\lambda / (\beta \cos \theta) \quad (1)$$

Where K = 0.94 (shape factor), λ = X-ray wavelength, β = full width at half maximum (FWHM) in radians [24], and θ = Bragg angle.

For ZnO hexagonal wurtzite structure, interplanar spacing dhkl and lattice parameters were determined using equation (2) [25]:

$$1/d^2hkl = (4/3) [(h^2 + hk + k^2) /a^2] + l^2/c^2 \quad (2)$$

Parameter c was extracted from (002) reflection (Eq. 3) :

$$c = dhkl \times l \quad (3)$$

Parameter a was calculated from (100) reflection (Eq. 4) [25]:

$$a = \lambda / (\sqrt{3} \times \sin \theta_{100}) \quad (4)$$

For P3HT orthorhombic structure, the general relationship is (Eq. 5) :

$$1/d^2hkl = h^2/a^2 + k^2/b^2 + l^2/c^2 \quad (5)$$

Parameter a (interlamellar spacing) was determined from (100) reflection (Eq. 6) [26],[27]:

$$a = \lambda / (2 \sin \theta_{100}) \quad (6)$$

Lattice strain (ε) was determined from peak broadening (Eq. 7) [28] :

$$\varepsilon = \beta \cos \theta / 4 \quad (7)$$

Dislocation density (δ) was estimated as (Eq. 8) [29] :

$$\delta = 1 / D^2 \quad (8)$$

XRD patterns were analyzed using HighScore Plus software for peak identification and profile fitting. Quantitative structural parameters were calculated from experimental XRD data using

custom Python scripts implementing equations (1)-(8).

4.2 Morphological Characterization

Surface morphology was examined using scanning electron microscopy (SEM) with field emission gun operating at 15 kV accelerating voltage [30],[31]. Samples were sputter-coated with thin gold layer (~5 nm) to prevent charging effects. Multiple magnifications (127× to 1.37k×) enabled comprehensive surface evaluation including grain structure, film continuity, and defect analysis.

4.3 Optical Characterization

Optical transmission spectra were recorded using UV-Vis spectrophotometer over 300-800 nm wavelength range with 1 nm resolution. Bare glass substrates served as baseline reference. Optical bandgap values were determined from Tauc plot analysis for direct transitions (Eq. 9) [32–35]:

$$(\alpha h\nu)^2 = A(h\nu - Eg) \quad (9)$$

Where α = absorption coefficient, h = Planck's constant, ν = photon frequency, A = material constant, and Eg = optical bandgap. For direct band gap semiconductors, the exponent n = ½ [33],[34]. Linear extrapolation of $(\alpha h\nu)^2$ versus photon energy ($h\nu$) to zero absorption yields bandgap energy [35].

Refractive index (n) was calculated using Herve-Vandamme relation (Eq. 10) [36–38]:

$$n = \sqrt{[1 + (A/(Eg + B))^2]} \quad (10)$$

With A = 13.6 and B = 3.4 eV [38],[39].

5. Results and Discussion

5.1 Structural Characterization of ZnO Thin Films

a. Phase Identification and Crystallinity Evolution

Figure 7 presents XRD patterns for ZnO films with varying layer numbers (4, 6, 8, 10) alongside JCPDS reference card 036-1451 for hexagonal wurtzite ZnO. All diffraction patterns exhibit characteristic reflections corresponding to (100), (002), (101), (102), (110), (103), (200), and (112) crystallographic planes, confirming polycrystalline hexagonal wurtzite phase formation.

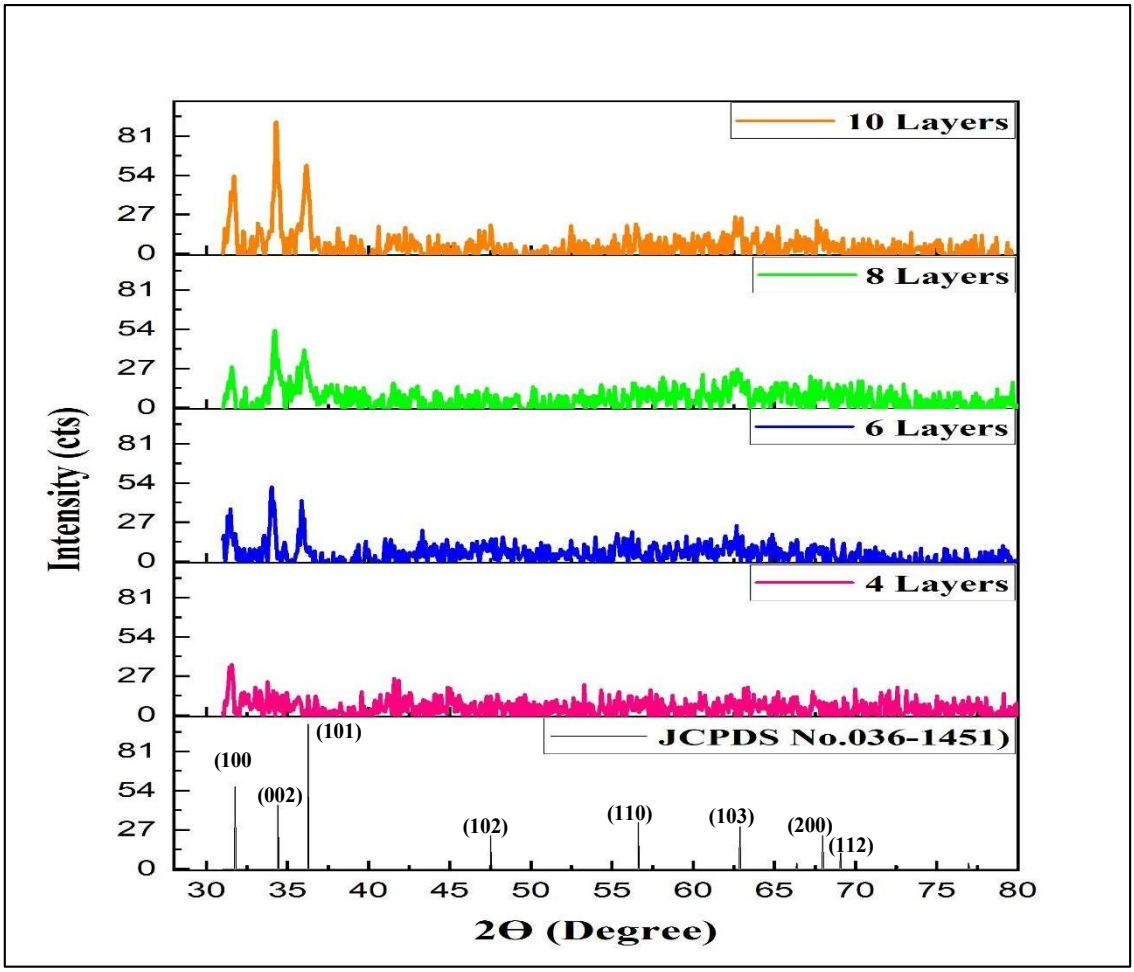

Figure 7 : XRD patterns of ZnO thin films with 4, 6, 8, and 10 layers, alongside the JCPDS reference for hexagonal wurtzite ZnO (card No. 036-1451).

The dominant (002) reflection at $2\theta \approx 34°$ indicates preferential c-axis orientation perpendicular to substrate surface, favorable for vertical charge transport in photovoltaic applications. Progressive intensity enhancement of all diffraction peaks with increasing layer number demonstrates systematic crystallinity improvement. The 4-layer sample exhibits relatively weak diffraction intensity indicating limited crystalline ordering, consistent with insufficient material thickness for complete crystal development. Increasing to 6 and 8 layers produces substantial peak intensity enhancement, with the 8-layer configuration displaying maximum crystallinity evidenced by sharpest, most intense diffraction features. The 10-layer sample, while maintaining crystallinity, shows slight intensity reduction and peak broadening compared to 8 layers, suggesting onset of stress-induced structural degradation.

b. Quantitative Structural Analysis

Table 1 summarizes quantitative structural parameters extracted from XRD data. The (002) peak position shifts systematically from 33.77° (4 layers) to 34.33° (10 layers), indicating lattice parameter evolution with thickness. Lattice parameter c calculated from (002) reflection decreases from 5.304 Å to 5.222 Å, while parameter a from (100) reflection decreases from 3.285 Å to 3.257 Å with increasing layers, suggesting gradual lattice contraction and stress evolution.

Table 1. Structural parameters of ZnO thin films as function of layer number

Layers	2θ(002) [°]	2θ(100) [°]	FWHM [°]	D [nm]	ε [$\times 10^{-3}$]	d_{002} [Å]	c [Å]	a [Å]	δ [$\times 10^{11}$ cm^{-2}]
4	33.770	31.428	0.354	24.5	5.0	2.625	5.304	3.285	1.66
6	34.025	31.480	0.268	33.0	3.7	2.633	5.266	3.280	0.92
8	34.205	31.570	0.242	36.1	3.4	2.620	5.240	3.270	0.77
10	34.325	31.698	0.298	29.7	4.1	2.611	5.222	3.257	1.13

Note : Peak positions (2θ) and FWHM values were extracted from XRD patterns using HighScore Plus software. Structural parameters (D, ε, c, a, δ) were calculated from experimental data using Python-based computational routines implementing equations (1) -(8).

Crystallite size evolution displays non-monotonic behavior with layer number. Starting from 24.5 nm (4 layers), grain size increases progressively to maximum value of 36.1 nm at 8 layers, followed by decrease to 29.7 nm for 10 layers. This trend reflects competing mechanisms : initial thickness increase facilitates crystallite coalescence and growth, while excessive thickness introduces stress accumulation and defect formation inhibiting further grain development.

Microstrain exhibits inverse correlation with crystallite size, consistent with Williamson-Hall relationship. Minimum strain (3.4×10^{-3}) coincides with maximum crystallite size (8 layers), indicating optimal structural quality with minimal lattice distortion. The 4-layer configuration experiences highest strain (5.0×10^{-3}) due to incomplete film formation, dominant substrate-induced stress, and constrained grain growth. While 6 layers shows improvement (3.7×10^{-3}), the 10-layer sample exhibits strain increase (4.1×10^{-3}) attributable to stress accumulation from excessive thickness.

Dislocation density, representing defect concentration, follows strain trends : 7.7×10^{10} cm^{-2} minimum for 8 layers versus 1.66×10^{11} cm^{-2} for 4 layers. Lower dislocation density indicates superior crystalline quality with fewer structural defects beneficial for charge carrier transport.

The observed trends align with established thin film growth mechanisms. Initially, increasing

thickness promotes crystallite coalescence through Ostwald ripening and secondary grain growth, reducing defect density and strain [13],[40–42]. However, beyond critical thickness (~8 layers, estimated ~400 nm), stress accumulation from thermal expansion mismatch, intrinsic film stress, and grain boundary interactions dominates, causing structural degradation despite increased material volume [43]–[45].

c. Morphological Characterization of ZnO Films

SEM analysis provides complementary morphological insights supporting XRD findings. **Figure 8** compares surface morphology of 8-layer (optimal) and 4-layer (sub-optimal) ZnO films at equivalent magnification.

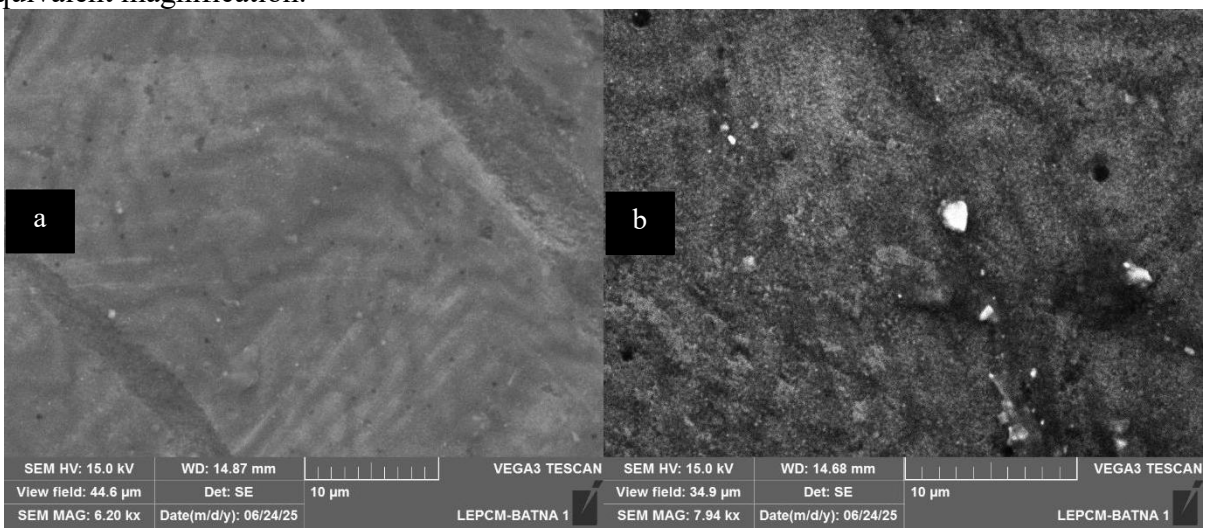

Figure 8: Scanning electron microscopy (SEM) images of ZnO thin films with different layer numbers : (a) 8-layer sample, (b) 4-layer.

The 8-layer configuration (Figure 8a) exhibits dense, homogeneous surface comprised of well-defined, uniformly distributed grains with minimal voids or discontinuities. The compact morphology indicates complete substrate coverage with good intergranular connectivity, favorable for efficient electron transport. Grain boundaries appear well-defined, suggesting high crystalline quality consistent with maximum crystallite size and minimum strain observed by XRD. Conversely, the 4-layer film, as seen in Figure 8b, displays rougher, more heterogeneous morphology with irregular grain shapes, visible voids, and incomplete surface coverage. These features indicate insufficient material thickness for continuous film formation and uniform grain development [46],[47]. The fragmented, porous structure would impede charge transport and promote recombination, explaining inferior optoelectronic performance.

The morphological evolution confirms that 8 ZnO layers provide optimal balance between film continuity, grain development, and surface homogeneity [48], while fewer layers yield discontinuous coverage and excessive layers may introduce microcracking or surface roughness from stress accumulation.

d. Optical Properties of ZnO Films

Transmission Spectroscopy

Window layers play a crucial role in solar cells by allowing sunlight to pass through to the active layer while ensuring good electrical conductivity. ZnO, as a wide bandgap semiconductor (~3.3 eV), exhibits high transparency in the visible range with typical transmittance of 85-90% [49]. For optimal window layer performance, maximizing the electrical conductivity to optical absorption ratio is essential [49].

Figure 9 presents UV-Vis transmission spectra for ZnO films with varying layer numbers deposited on glass substrates. All samples exhibit characteristic semiconductor optical behavior: strong UV absorption below ~380 nm due to fundamental bandgap absorption, followed by high transparency throughout visible range (400-800 nm) exceeding 90% [1–3]. This strong UV absorption region is directly related to ZnO's wide bandgap nature [13].

Figure 9 : UV-Vis Transmittance Spectra of Zinc Oxide (ZnO) Films Deposited on Glass

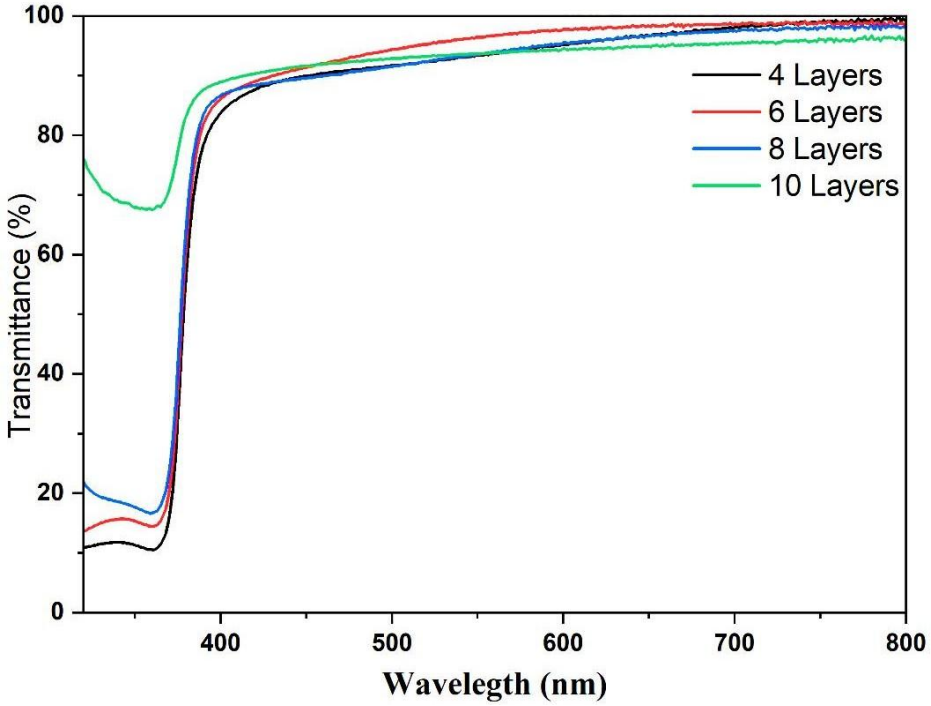

Substrates with Different Numbers of Layers (4, 6, 8, and 10).

Transmission values at 800 nm decrease systematically with layer number: 99.3% (4 layers), 98.8% (6 layers), 98.0% (8 layers), and 96.3% (10 layers). This trend reflects increased optical path length and potential light scattering from enhanced film thickness, with transmittance reduction from 99% to 96% correlating with improved crystalline nature as observed in previous works [50]–[52]. Notably, all configurations maintain excellent transparency (>96%), satisfying window layer requirements for solar cells.

The 10-layer sample exhibits anomalous UV transmission enhancement (~60-70% vs. ~20-25% for 4, 6, and 8-layer films in the 300-380 nm range), suggesting structural deterioration such as increased porosity, microcracking, or phase inhomogeneity allowing more UV penetration. This lower UV absorption represents a disadvantage for solar cell applications, as it is desirable for window films to block UV radiation to protect the active layer. This observation aligns with structural degradation evidenced by XRD and emphasizes that excessive thickness compromises both structural and optical quality.

Among the studied samples, the 4-layer ZnO film exhibits the highest transmittance at 800 nm (99.25%), which may initially appear optically ideal. However, such extremely high transmittance often indicates a film that is too thin or discontinuous, potentially leading to poor electrical conduction, uncovered micro-regions, and non-uniform contact with adjacent layers. The 6-layer sample offers similarly high transmittance (98.78%) while providing better film continuity, representing an optimal balance between optical transparency and electrical conductivity. The 8-layer film, with transmittance of 98.02%, remains well within the optimal range for photovoltaic window layers. Crucially, XRD and SEM characterizations reveal that the 8-layer configuration yields the highest crystallinity and most favorable surface morphology features that significantly outweigh the minor transmittance reduction compared to the 4-layer film. Conversely, the 10-layer film shows more marked decline in transmittance (96.29%), which may result from increased internal defects, porosity, microcracks, or mechanical stress factors detrimental to window layer function in solar cells.

Optical Bandgap Analysis

The optical bandgap (Eg) represents a fundamental property of semiconductors, defining the minimum energy required to excite an electron from the valence band to the conduction band. This parameter is crucial for understanding the optoelectronic behavior and charge carrier dynamics in thin films.

Optical bandgaps determined from Tauc plot analysis reveal systematic variation with layer number as listed in Table 2. The Tauc plot method, based on plotting $(\alpha h\nu)^2$ versus photon energy ($h\nu$) for direct band gap materials, enables accurate bandgap determination through linear extrapolation to the energy axis where $(\alpha h\nu)^2 = 0$ [32]–[35].

Bandgap increases from 3.319 eV (4 layers) to maximum 3.335 eV (8 layers), then slightly decreases to 3.328 eV (10 layers). The average bandgap value across all samples is 3.32 eV, consistent with reported values for ZnO thin films. This systematic increase from 3.319 eV to 3.335 eV in the range of 4-8 layers correlates with improvement in crystal quality observed through XRD analysis.

Table 2 : Optical properties of ZnO thin films

Layers	Eg [eV]	n	T_{800} [%]
4	3.319	2.260	99.3
6	3.322	2.257	98.8
8	3.335	2.255	98.0
10	3.328	2.255	96.3

Bandgap widening with improved crystallinity (4→8 layers) reflects quantum confinement effects in smaller grains and reduced defect-induced band tailing. Maximum bandgap at 8 layers correlates with optimal crystallinity and minimum strain observed in XRD analysis, confirming the strong relationship between structural and optical properties. The slight decrease for 10 layers aligns with structural degradation and increased defect density.

Refractive Index

Optical and electronic behavior of semiconductors are fundamentally determined by two key properties: energy gap and refractive index [53]. The refractive index provides crucial information about light propagation and interaction within the material.

Refractive index, calculated via Herve-Vandamme relation (Eq. 10), exhibits inverse correlation with bandgap (Table 2), decreasing from 2.260 to 2.255 with increasing layer number from 4 to 8 layers. This inverse relationship between refractive index and bandgap is consistent with fundamental optical physics: materials with smaller bandgap energy possess larger refractive index values [53],[54]. The observed decrease in refractive index with increasing bandgap confirms the improved crystalline quality and reduced defect density in optimized films, as defects typically contribute to bandgap narrowing and refractive index enhancement.

5.2 Structural Characterization of P3HT Thin Films

a. Crystalline Phase Evolution

Figure 10 presents XRD patterns for P3HT films with 2-5 layers alongside JCPDS reference 00-052-2366 for orthorhombic P3HT. The dominant (100) reflection at $2\theta \approx 5.1°$ corresponds to lamellar d-spacing of ~17-18 Å, representing interchain distance in P3HT's edge-on molecular orientation critical for vertical charge transport [27],[55]. Higher-order reflections (200) and (300) appear in well-ordered samples, indicating long-range structural coherence.

Figure 10 : XRD patterns of P3HT thin films with 2, 3, 4, and 5 layers, alongside the JCPDS reference for orthorhombic P3HT (card No. 00-052-2366).

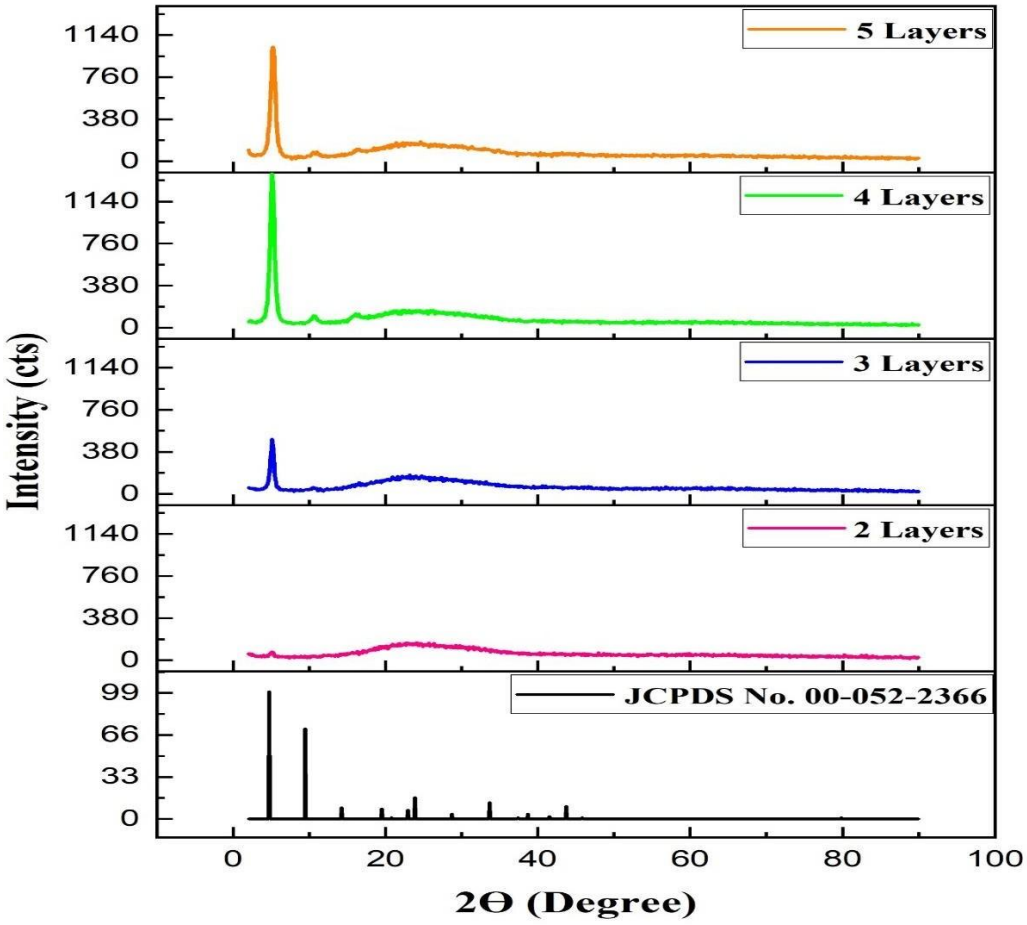

The 2-layer configuration exhibits negligible crystallinity with barely detectable diffraction, indicating insufficient thickness for effective molecular self-assembly and π-π stacking. Three layers develop moderate crystallinity with (100) peak intensity of 507 cts, confirming emergence of lamellar ordering characteristic of semi-crystalline P3HT [56]. Maximum crystallinity occurs

at 4 layers (1386 cts), representing optimal balance between material quantity enabling self-organization and avoiding thickness-induced disorder [57],[58]. The appearance of well-defined (200) and (300) reflections in the 4-layer sample evidences significant enhancement of long-range crystalline order. Five layers show 22% intensity reduction (1084 cts) versus 4 layers, suggesting crystalline degradation from stress accumulation or morphological deterioration [59],[60].
These results align well with established literature on P3HT crystallization behavior and thickness-dependent structural evolution [56].

b. Quantitative Structural Analysis

Table 3 summarizes structural parameters for P3HT films. Crystallite size decreases systematically from 15.4 nm (3 layers) to 11.5 nm (5 layers) while microstrain increases from 1.0×10^{-3} to 1.2×10^{-3}, indicating progressive structural degradation despite increased material quantity.

Table 3 : Structural parameters of P3HT thin films

Layers	2θ(100) [°]	FWHM [°]	D [nm]	ε [$\times10^{-3}$]	d_{100} [Å]	a [Å]	δ [$\times10^{11}$ cm^{-2}]
2	-	-	-	-	-	-	-
3	5.111	0.652	12.2	1.13	17.27	17.27	6.7
4	5.119	0.515	15.4	1.00	17.25	17.25	4.2
5	5.217	0.688	11.5	1.20	16.93	16.93	7.6

Lattice parameter a remains stable (~17.25-17.27 Å) for 3-4 layers, then contracts to 16.93 Å for 5 layers, indicating compressive stress development [61],[62]. Dislocation density increases dramatically from 4.2×10^{11} cm^{-2} (optimal 4 layers) to 7.6×10^{11} cm^{-2} (5 layers), confirming enhanced structural disorder.
The inverse correlation between crystallite size and strain reflects competing mechanisms in polymer thin films: initial thickness increase facilitates molecular ordering through extended relaxation time and reduced substrate influence, while excessive thickness introduces chain entanglement, increased grain boundaries, and mechanical stress hindering optimal crystallization [63],[64].

c. Morphological Characterization of P3HT Films

SEM characterization of optimal 4-layer P3HT films (**Figure 11**) reveals excellent morphological quality. Low magnification (127×, field of view 2.18 mm) shows continuous, homogeneous coverage without voids, cracks, or delamination, confirming complete substrate coverage. High

magnification (1.37k×, field of view 203 µm) reveals moderately textured surface with submicron fibrillar/globular structures characteristic of semi-crystalline P3HT. Absence of aggregates or pinholes indicates uniform deposition quality.

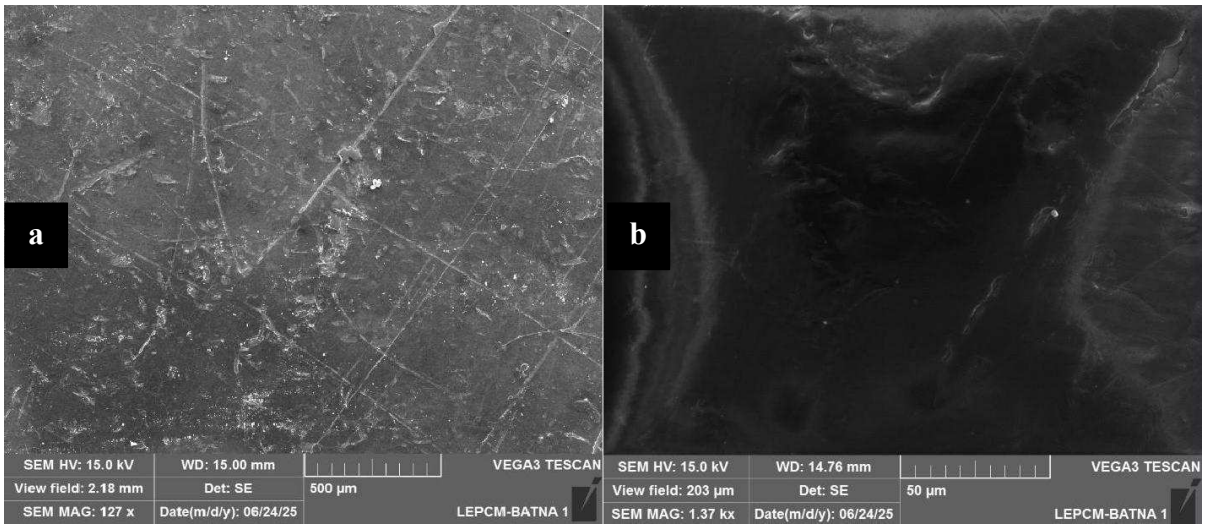

Figure 11 : SEM characterization of 4-layer P3HT film on glass substrate (a) Low-magnification view (127× ; field of view ~2.18 mm), (b) High-magnification view (1.37 k× ; field of view ~203 µm).

The smooth, ordered surface morphology correlates with maximum XRD crystallinity, confirming that 4-layer configuration achieves optimal balance between structural order and surface quality necessary for efficient charge transport in photovoltaic devices. The observation that P3HT films reach maximum crystallinity at an intermediate thickness followed by decline in structural order in thicker assemblies finds strong support in recent studies. A 2024 investigation comparing various coating techniques concluded that optimal lamellar stacking occurs at moderate thicknesses, while thicker films exhibit increased disorder and reduced crystallinity [65].

5.3 Optimal Heterostructure Architecture

Integration of structural, morphological, and optical characterization establishes ZnO (8 layers) /P3HT (4 layers) as optimal hybrid architecture :

- **ZnO optimization (8 layers) :**

Maximum crystallite size (36.1 nm) and minimum strain (3.4×10^{-3})
Lowest dislocation density (7.7×10^{10} cm^{-2})
Highest optical bandgap (3.335 eV)

Excellent transparency (98.0% at 800 nm)
Dense, homogeneous surface morphology

- **P3HT optimization (4 layers) :**

Maximum (100) diffraction intensity (1386 cts)
Optimal crystallite size (15.4 nm) and minimum strain (1.0×10^{-3})
Lowest dislocation density (4.2×10^{11} cm^{-2})
Continuous, defect-free surface morphology
Optimal lamellar organization (d-spacing 17.25 Å)
This configuration maximizes light absorption in P3HT active layer while maintaining excellent electron extraction through high-quality ZnO window layer, establishing foundation for high-performance hybrid photovoltaic devices.

- **Heterostructure Fabrication Strategy**

To address thermal incompatibility between ZnO and P3HT processing requirements, a thermally-separated two-step fabrication protocol was implemented :
Step 1 : ZnO layers (8 layers optimal) were deposited on glass substrates and calcined at 450°C to achieve complete crystallization and organic residue removal. Kapton tape masking defined contact regions (**Figure 12**).

Figure 12 : Masking of the ZnO layer with Kapton tape to define the front contact area.

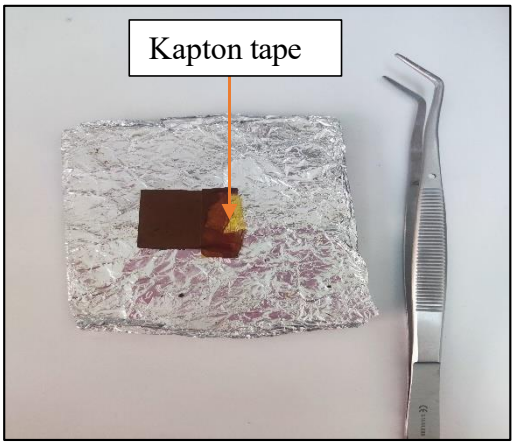

Step 2 : P3HT layers (4 layers optimal) were subsequently deposited on calcined ZnO films with thermal treatment limited to 130°C maximum, preserving polymer integrity while optimizing morphology **Figure 13**.

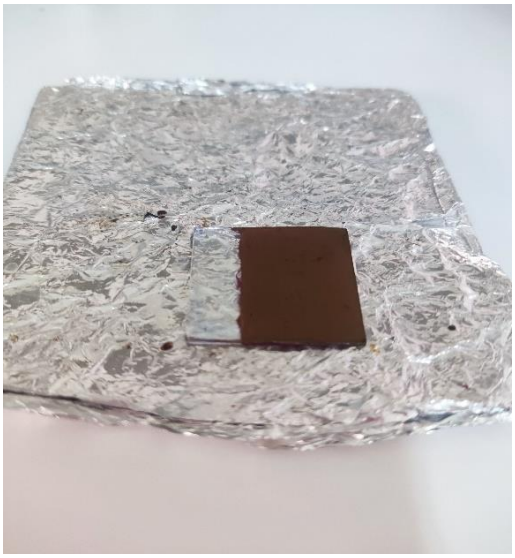

Figure 13 : The prepared thin film based on the optimal layer configuration for the hybrid solar cell (ZnO/P3HT).

This sequential approach ensures optimal ZnO crystallinity while protecting thermally-sensitive P3HT from degradation.

6. Conclusion

This work successfully establishes a systematic optimization methodology for ZnO/P3HT hybrid heterostructure solar cells by comprehensively investigating the influence of layer number on structural, morphological, and optical properties. We first demonstrated that optimal material quality depends critically on layer thickness : eight layers of ZnO were found to yield the best crystalline quality (grain size of 36.1 nm), superior optical transmission (T > 98%, Eg = 3.335 eV), and dense morphology, while the P3HT active layer achieved maximum lamellar ordering and optimal crystallinity with four layers. Furthermore, a thermally-separated fabrication protocol was validated, effectively resolving the conflicting processing requirements by allowing ZnO high-temperature calcination (450°C) to ensure optimal crystallinity prior to the low-temperature processing 130°C of the P3HT film. The non-monotonic evolution of crystallinity with thickness elucidated the competing mechanisms between grain growth facilitation and stress accumulation, establishing critical thickness windows for high-quality film growth. The resulting ZnO (8 layers) P3HT (4 layers) architecture provides crucial, evidence-based design principles for high-performance organic-inorganic photovoltaic devices. Future research should leverage these optimized material configurations for complete device integration, focusing on interface engineering, electrical contact optimization, and detailed characterization of power conversion

efficiency under standard test conditions.

ACKNOWLEDGMENTS
The work is included in the PRFU project under contract number B00L02UN310220220001 Oran University of sciences and technology USTO-MB. The authors acknowledge Professor Noureddine Sengouga (LMSM Laboratory, University of Biskra) for providing access to experimental facilities and technical support. Special thanks to Engineer Youcef Bahloul for technical assistance.

Contributions

Author contributions

L. M.: Conceptualization, Discussions, Data curation, Resources (SCAPS simulations and material parameters), Validation (physical), Writing, review & editing.

M. B.: Conceptualization, Methodology, Supervising, Writing original draft Reviewing and Editing, Resources, Discussions, Interpretation of results

M.A. S.: Conceptualization, Methodology (ML pipeline, PSO), Software, Formal analysis, Visualization, Discussions, Writing original draft.

K. D.: Discussions, Interpretation, Design

A. A.: Conceptualization, Methodology, Supervising, formal analysis, validation, visualization, experimental design

FUNDING
This work was supported by ongoing institutional funding. No additional grants to carry out or direct this particular research were obtained.

CONFLICT OF INTEREST
The authors of this work declare that they have no conflicts of interest.

References

[1] Snaith, H. J. "Perovskites: The Emergence of a New Era for Low-Cost, High-Efficiency Solar Cells" ,*Journal of Physical Chemistry Letters* ,*4* (21), pp. 3623–3630, 2013. https://doi.org/10.1021/JZ4020162.

[2] Lewis, N. S.,Nocera, D. G. "Powering the Planet: Chemical Challenges in Solar Energy Utilization" ,*Proc Natl Acad Sci U S A* ,*103* (43), pp. 15729–15735, 2006. https://doi.org/10.1073/PNAS.0603395103;WGROUP:STRING:PUBLICATION.

[3] Smestad, G. P. "Education and Solar Conversion:: Demonstrating Electron Transfer" ,*Solar Energy Materials and Solar Cells* ,*55* (1–2), pp. 157–178, 1998.

https://doi.org/10.1016/S0927-0248(98)00056-7.
[4] Reddy, P. K.,Goutam, P. J.,Dilip, K. S.,Ghoshal, A. K.,Iyer, P. K. "Mechanistic Investigation, Kinetic Modeling and Analysis Parameters of Poly(3-Hexylthiophene) Degradation to Fullerenes" ,*Polym Degrad Stab* ,*94* (10), pp. 1839–1848, 2009. https://doi.org/10.1016/J.POLYMDEGRADSTAB.2009.05.018.
[5] Iakobson, O. D.,Gribkova, O. L.,Tameev, A. R.,Nunzi, J. M. "A Common Optical Approach to Thickness Optimization in Polymer and Perovskite Solar Cells" ,*Scientific Reports 2021 11:1* ,*11* (1), pp. 5005-, 2021. https://doi.org/10.1038/s41598-021-84452-x.
[6] Xie, Y.,Gao, S.,Eslamian, M. "Fundamental Study on the Effect of Spray Parameters on Characteristics of P3HT:PCBM Active Layers Made by Spray Coating" ,*Coatings 2015, Vol. 5, Pages 488-510* ,*5* (3), pp. 488–510, 2015. https://doi.org/10.3390/COATINGS5030488.
[7] Chapin, D. M.,Fuller, C. S.,Pearson, G. L. "A New Silicon P-n Junction Photocell for Converting Solar Radiation into Electrical Power ARTICLES YOU MAY BE INTERESTED IN" ,*J Appl Phys* ,*25*, pp. 676, 1954. https://doi.org/10.1063/1.1721711.
[8] Brooks, W. S. M.,Lamb, D. A.,Irvine, S. J. C. "IR Reflectance Imaging for Crystalline Si Solar Cell Crack Detection" ,*IEEE J Photovolt* ,*5* (5), pp. 1271–1275, 2015. https://doi.org/10.1109/JPHOTOV.2015.2438636.
[9] Gischkat, T.,Schachtler, D.,Stevanovic, I.,Balogh-michels, Z.,Botha, R.,Bächli, A.,Cucinelli, M.,Mocker, A.,Gutsche, M.,Günther, S.,Alder, P.,Eiermann, B. "Substrate Cleaning Processes and Their Influence on the Laser Resistance of Anti-Reflective Coatings" ,*Applied Sciences 2020, Vol. 10, Page 8496* ,*10* (23), pp. 8496, 2020. https://doi.org/10.3390/APP10238496.
[10] Ames, D. P.,Chelli, S. J. "Surface Contamination Effects on Film Adhesion on Metals and Organic Polymers" ,*Surf Coat Technol* ,*187* (2–3), pp. 199–207, 2004. https://doi.org/10.1016/J.SURFCOAT.2004.03.027.
[11] Mustafa, H. A.,Jameel, D. A. "Modeling and the Main Stages of Spin Coating Process: A Review" ,*Journal of Applied Science and Technology Trends* ,*2* (02), pp. 119–123, 2021. https://doi.org/10.38094/jastt203109.
[12] Elsayed, I. A.,Afify, A. S. "Controlling the Surface Morphology of ZnO Nano-Thin Film Using the Spin Coating Technique" ,*Materials 2022, Vol. 15, Page 6178* ,*15* (17), pp. 6178, 2022. https://doi.org/10.3390/MA15176178.
[13] Khan, M. I.,Bhatti, K. A.,Qindeel, R.,Alonizan, N.,Althobaiti, H. S. "Characterizations of Multilayer ZnO Thin Films Deposited by Sol-Gel Spin Coating Technique" ,*Results Phys* ,*7*, pp. 651–655, 2017. https://doi.org/10.1016/J.RINP.2016.12.029.
[14] Pandey, A. K.,Rahim, N. A.,Hasanuzzaman, M.,Pant, P. C.,Tyagi, V. V. "Solar Photovoltaics (PV): A Sustainable Solution to Solve Energy Crisis" ,*Green Technologies and Environmental Sustainability* ,pp. 157–178, 2017. https://doi.org/10.1007/978-3-319-50654-8_7.
[15] Wadia, C.,Alivisatos, A. P.,Kammen, D. M. "Materials Availability Expands the Opportunity for Large-Scale Photovoltaics Deployment" ,*Environ Sci Technol* ,*43* (6), pp. 2072–2077, 2009. https://doi.org/10.1021/ES8019534.
[16] Rühle, S.,Shalom, M.,Zaban, A. "Quantum-Dot-Sensitized Solar Cells" ,*ChemPhysChem* ,*11* (11), pp. 2290–2304, 2010. https://doi.org/10.1002/CPHC.201000069;REQUESTEDJOURNAL:JOURNAL:14397641;PAGEGROUP:STRING:PUBLICATION.
[17] Askariyya, J.,Aprilia, A.,Riveli, N.,Safriani, L. "The Effect of Calcination Temperature on ZnO Crystals Based on Emission Spectrum from Photoluminescence Characterization" ,*JIIF (Jurnal Ilmu dan Inovasi Fisika)* ,*9* (1), pp. 43–55, 2025. https://doi.org/10.24198/JIIF.V9I1.60621.
[18] Holliday, S.,Ashraf, R. S.,Wadsworth, A.,Baran, D.,Yousaf, S. A.,Nielsen, C. B.,Tan, C. H.,Dimitrov, S. D.,Shang, Z.,Gasparini, N.,Alamoudi, M.,Laquai, F.,Brabec, C. J.,Salleo, A.,Durrant, J. R.,McCulloch, I. "High-Efficiency and Air-Stable P3HT-Based Polymer Solar

Cells with a New Non-Fullerene Acceptor" ,*Nature Communications 2016 7:1* ,*7* (1), pp. 11585-, 2016. https://doi.org/10.1038/ncomms11585.
[19] Reddy, P. K.,Goutam, P. J.,Dilip, K. S.,Ghoshal, A. K.,Iyer, P. K. "Mechanistic Investigation, Kinetic Modeling and Analysis Parameters of Poly(3-Hexylthiophene) Degradation to Fullerenes" ,*Polym Degrad Stab* ,*94* (10), pp. 1839–1848, 2009. https://doi.org/10.1016/J.POLYMDEGRADSTAB.2009.05.018.
[20] Bunaciu, A. A.,Udriştioiu, E. gabriela,Aboul-Enein, H. Y. "X-Ray Diffraction: Instrumentation and Applications" ,*Crit Rev Anal Chem* ,*45* (4), pp. 289–299, 2015. https://doi.org/10.1080/10408347.2014.949616.
[21] *X-ray Diffraction (XRD) - Overview | Malvern Panalytical*. https://www.malvernpanalytical.com/en/products/technology/xray-analysis/x-ray-diffraction (accessed 2025-12-13).
[22] Messick, J. "The History of the International Centre for Diffraction Data" ,*Powder Diffr* ,*27* (1), pp. 36–44, 2012. https://doi.org/10.1017/S0885715612000085.
[23] of Geosciences, D.,Brook University, S. "Stony Brook University Department of Geosciences 2009 Year in Review".
[24] Fatimah, S.,Ragadhita, R.,Al Husaeni, D. F.,Nandiyanto, A. B. D. "How to Calculate Crystallite Size from X-Ray Diffraction (XRD) Using Scherrer Method" ,*ASEAN Journal of Science and Engineering* ,*2* (1), pp. 65–76, 2022. https://doi.org/10.17509/AJSE.V2I1.37647.
[25] Mohamed Khider of Biskra, U.,Aya, L. "Elaboration of Pure and Doped ZnO Powders with the Sol Gel Method" ,2024.
[26] *Selective CO 2 adsorption and bathochromic shift in a phosphocholine-based lipid and conjugated polymer assembly - RSC Advances (RSC Publishing) DOI:10.1039/D2RA00453D*. https://pubs.rsc.org/en/content/articlehtml/2022/ra/d2ra00453d (accessed 2025-12-13).
[27] Kayunkid, N.,Uttiya, S.,Brinkmann, M. "Structural Model of Regioregular Poly(3-Hexylthiophene) Obtained by Electron Diffraction Analysis" ,*Macromolecules* ,*43* (11), pp. 4961–4967, 2010. https://doi.org/10.1021/MA100551M.
[28] Jayaram, P.,Pradyumnan, P. P.,Karazhanov, S. Z. "Micro-Strain, Dislocation Density and Surface Chemical State Analysis of Multication Thin Films" ,*Physica B Condens Matter* ,*501*, pp. 140–145, 2016. https://doi.org/10.1016/J.PHYSB.2016.08.018.
[29] Edalati, K.,Enikeev, N. "Dislocation Density in Ceramics Processed by Severe Plastic Deformation via High-Pressure Torsion" ,*Materials 2024, Vol. 17, Page 6189* ,*17* (24), pp. 6189, 2024. https://doi.org/10.3390/MA17246189.
[30] Aharinejad, S. H.,Lametschwandtner, A. "Fundamentals of Scanning Electron Microscopy" ,*Microvascular Corrosion Casting in Scanning Electron Microscopy* ,pp. 44–51, 1992. https://doi.org/10.1007/978-3-7091-9230-6_3.
[31] *Sample Preparation Handbook for Transmission Electron Microscopy: Techniques - Jeanne Ayache, Luc Beaunier, Jacqueline Boumendil, Gabrielle Ehret, Danièle Laub - Google Livres*. https://books.google.dz/books?hl=fr&lr=&id=XAl6Xd0cYIoC&oi=fnd&pg=PR7&dq=sample+preparation+handbook+for+transmission+electron+microscopy+techniques+springer+science&ots=OfrZNttKaY&sig=bQsNuh7LKmrNEvax5GhXSxKUMoc&redir_esc=y#v=onepage&q=sample%20preparation%20handbook%20for%20transmission%20electron%20microscopy%20techniques%20springer%20science&f=false (accessed 2025-12-13).
[32] Matsumoto, T.,Nishi, K.,Tamba, S.,Kotera, M.,Hongo, C.,Mori, A.,Nishino, T. "Molecular Weight Effect on Surface and Bulk Structure of Poly(3-Hexylthiophene) Thin Films" ,*Polymer (Guildf)* ,*119*, pp. 76–82, 2017. https://doi.org/10.1016/J.POLYMER.2017.05.027.
[33] Casalegno, M.,Famulari, A.,Meille, S. V. "Modeling of Poly(3-Hexylthiophene) and Its Oligomer's Structure and Thermal Behavior with Different Force Fields: Insights into the Phase Transitions of Semiconducting Polymers" ,*Macromolecules* ,*55* (7), pp. 2398–2412, 2022. https://doi.org/10.1021/ACS.MACROMOL.2C00131.
[34] Mexicana De Física, S.,México, A. C.,Morales, E.,Mora, S.,Pal, E. ;,Morales, A. E.,Mora, E.

S.,Pal, U. "Use of Diffuse Reflectance Spectroscopy for Optical Characterization of Un-Supported Nanostructures" ,*REVISTA MEXICANA DE F ´ ISICA S* ,*53* (5), pp. 18–22, 2007.
[35] Gutiérrez-Fernández, E.,Ezquerra, T. A.,Rebollar, E.,Cui, J.,Marina, S.,Martín, J.,Nogales, A. "Photophysical and Structural Modulation of Poly(3-Hexylthiophene) Nanoparticles via Surfactant-Polymer Interaction" ,*Polymer (Guildf)* ,*218*, pp. 123515, 2021. https://doi.org/10.1016/J.POLYMER.2021.123515.
[36] Tripathy, S. K. "Refractive Indices of Semiconductors from Energy Gaps" ,*Opt Mater (Amst)* ,*46*, pp. 240–246, 2015. https://doi.org/10.1016/J.OPTMAT.2015.04.026.
[37] Abdelkrim, A.,Rahmane, S.,Nabila, K.,Hafida, A.,Abdelouahab, O. "Polycrystalline SnO2 Thin Films Grown at Different Substrate Temperature by Pneumatic Spray" ,*Journal of Materials Science: Materials in Electronics 2016 28:6* ,*28* (6), pp. 4772–4779, 2016. https://doi.org/10.1007/S10854-016-6122-9.
[38] Hervé, P.,Vandamme, L. K. J. "General Relation between Refractive Index and Energy Gap in Semiconductors" ,*Infrared Phys Technol* ,*35* (4), pp. 609–615, 1994. https://doi.org/10.1016/1350-4495(94)90026-4.
[39] Abdelkrim, A.,Rahmane, S.,Abdelouahab, O.,Hafida, A.,Nabila, K. "Optoelectronic Properties of SnO2 Thin Films Sprayed at Different Deposition Times" ,*Chinese Physics B* ,*25* (4), pp. 046801, 2016. https://doi.org/10.1088/1674-1056/25/4/046801.
[40] Kaushik, V.,Bhardwaj, K.,Kumar, D.,Kumar, M.,Sharma, S. K. "Effect of Various Processing Parameters on the Properties of ZnO Thin Films" ,*Hybrid Advances* ,*7*, pp. 100295, 2024. https://doi.org/10.1016/J.HYBADV.2024.100295.
[41] Liu, Y. X.,Liu, Y. C.,Shen, D. Z.,Zhong, G. Z.,Fan, X. W.,Kong, X. G.,Mu, R.,Henderson, D. O. "Preferred Orientation of ZnO Nanoparticles Formed by Post-Thermal Annealing Zinc Implanted Silica" ,*Solid State Commun* ,*121* (9–10), pp. 531–536, 2002. https://doi.org/10.1016/S0038-1098(02)00006-6.
[42] Santos, A. M. P.,Santos, E. J. P. "High Quality C-Axis Oriented ZnO Thin-Film Obtained at Very Low Pre-Heating Temperature" ,*Mater Lett* ,*61* (16), pp. 3432–3435, 2006. https://doi.org/10.1016/j.matlet.2006.11.084.
[43] Nambiar, B.,Sadiku Emmanuel, R.,Babu Perumal, A.,Gartner, M.,Stroescu, H.,Mitrea, D.,Nicolescu, M. "Various Applications of ZnO Thin Films Obtained by Chemical Routes in the Last Decade" ,*Molecules 2023, Vol. 28, Page 4674* ,*28* (12), pp. 4674, 2023. https://doi.org/10.3390/MOLECULES28124674.
[44] Krysova, H.,Mansfeldova, V.,Tarabkova, H.,Pisarikova, A.,Hubicka, Z.,Kavan, L. "High-Quality Dense ZnO Thin Films: Work Function and Photo/Electrochemical Properties" ,*Journal of Solid State Electrochemistry* ,*28* (8), pp. 2531–2546, 2024. https://doi.org/10.1007/S10008-023-05766-6/FIGURES/8.
[45] Ayoub, I.,Kumar, V.,Abolhassani, R.,Sehgal, R.,Sharma, V.,Sehgal, R.,Swart, H. C.,Mishra, Y. K. "Advances in ZnO: Manipulation of Defects for Enhancing Their Technological Potentials" ,*Nanotechnol Rev* ,*11* (1), pp. 575–619, 2022. https://doi.org/10.1515/NTREV-2022-0035/XML.
[46] Chao, C.-H.,Wei, D.-H. "Synthesis and Characterization of High C-Axis ZnO Thin Film by Plasma Enhanced Chemical Vapor Deposition System and Its UV Photodetector Application" ,*Journal of Visualized Experiments* ,No. 104, pp. 53097, 2015. https://doi.org/10.3791/53097.
[47] Yergaliuly, G.,Soltabayev, B.,Kalybekkyzy, S.,others. "Effect of Thickness and Reaction Media on Properties of ZnO Thin Films by SILAR" ,*Sci Rep* ,*12* (1), pp. 851, 2022. https://doi.org/10.1038/s41598-021-82851-z.
[48] Johari, S.,Muhammad, N. Y.,Zakaria, M. R. "Study of Zinc Oxide Thin Film Characteristics". In *EPJ Web of Conferences*; EDP Sciences, 2017; Vol. 162, p 1057. https://doi.org/10.1051/epjconf/201716201057.
[49] Fuhs, W. "ZnO Window Layers for Solar Cells" ,*Zinc Oxide—A Material for Micro-and Optoelectronic Applications* ,*194*, pp. 197–209, 2005.

[50] Arif, M.,Sanger, A.,Vilarinho, P. M.,Singh, A. "Effect of Annealing Temperature on Structural and Optical Properties of Sol–Gel-Derived ZnO Thin Films" ,*J Electron Mater* ,*47* (7), pp. 3678–3684, 2018.
[51] Chaitra, U.,Kekuda, D.,Mohan Rao, K. "Effect of Annealing Temperature on the Evolution of Structural, Microstructural, and Optical Properties of Spin Coated ZnO Thin Films" ,*Ceram Int* ,*43* (9), pp. 7115–7122, 2017. https://doi.org/10.1016/j.ceramint.2017.02.141.
[52] Ivanova, T.,Harizanova, A.,Koutzarova, T.,Vertruyenc, B. "Study of ZnO Sol-Gel Films: Effect of Annealing" ,*Mater Lett* ,*64*, pp. 1371–1374, 2010. https://doi.org/10.1016/j.matlet.2010.03.035.
[53] Hervé, P.,Vandamme, L. K. J. "General Relation between Refractive Index and Energy Gap in Semiconductors" ,*Infrared Phys Technol* ,*35*, pp. 609, 1994. https://doi.org/10.1016/1350-4495(94)90026-4.
[54] Allag, A.,Rahmane, S.,Ouahab, A.,Attouche, H.,Kouidri, N. "Optoelectronic Properties of SnO_2 Thin Films Sprayed at Different Deposition Times" ,*Chinese Physics B* ,*25* (4), pp. 46801, 2016. https://doi.org/10.1088/1674-1056/25/4/046801.
[55] Noh, J.,Koo, D. G.,Hyun, C.,Lee, D.,Jang, S.,Kim, J.,Jeon, Y.,Moon, S.-Y.,Chae, B.,Nam, I. "Selective CO 2 Adsorption and Bathochromic Shift in a Phosphocholine-Based Lipid and Conjugated Polymer Assembly" ,*RSC Adv* ,*12* (14), pp. 8385–8393, 2022.
[56] Sirringhaus, H.,Brown, P. J.,Friend, R. H.,others. "Two-Dimensional Charge Transport in Self-Organized, High-Mobility Conjugated Polymers" ,*Nature* ,*401* (6754), pp. 685–688, 1999. https://doi.org/10.1038/44359.
[57] Zen, A.,Pflaum, J.,Hirschmann, S.,others. "Effect of Molecular Weight and Annealing of Poly(3-Hexylthiophene)s on the Performance of Organic Field-Effect Transistors" ,*Adv Funct Mater* ,*14* (8), pp. 757–764, 2004. https://doi.org/10.1002/adfm.200305414.
[58] Prosa, T. J.,Winokur, M. J.,Moulton, J.,others. "X-Ray Structural Studies of Poly(3-Alkylthiophenes): An Example of an Inverse Comb" ,*Macromolecules* ,*25* (17), pp. 4364–4372, 1992. https://doi.org/10.1021/ma00051a030.
[59] Miller, A. M. "Synthesis and Characterization of Transition Metal Dichalcogenide Heterostructures", University of Oregon, 2022.
[60] Rivnay, J.,others. "Organic Electrochemistry" ,*Chem Rev* ,*112* (10), pp. 5488–5519, 2012. https://doi.org/10.1021/cr200273n.
[61] Kline, R. J.,McGehee, M. D. "Morphology and Charge Transport in Conjugated Polymers" ,*Journal of Macromolecular Science, Part C: Polymer Reviews* ,*46* (1), pp. 27–45, 2006. https://doi.org/10.1081/MC-200031726.
[62] Müller, C.,Aghamohammadi, M.,Himmelberger, S.,others. "One-Step Macroscopic Alignment of Conjugated Polymer Systems by Epitaxial Crystallization during Spin-Coating" ,*Adv Funct Mater* ,*23* (19), pp. 2368–2377, 2013. https://doi.org/10.1002/adfm.201202715.
[63] Ungár, T. J. S. M. "Microstructural Parameters from X-Ray Diffraction Peak Broadening" ,*Scr Mater* ,*51* (8), pp. 777–781, 2004. https://doi.org/10.1016/j.scriptamat.2004.05.007.
[64] Chabinyc, M. L. "X-Ray Scattering from Films of Semiconducting Polymers" ,*Polymer Reviews* ,*48* (3), pp. 463–492, 2008. https://doi.org/10.1080/15583720802231734.
[65] Molefe, F. V,Mothudi, B. M.,Dhlamini, M. S. "The Effect of Deposition Method and Thickness Dependence on the Growth of P3HT for Organic Photovoltaic Devices" ,*Results in Optics* ,*16*, pp. 100684, 2024. https://doi.org/10.1016/j.rio.2024.100684.